 CMES, vol.1, no.1, pp.11-25, 2006

Three-Dimensional Dynamic Fracture Analysis Using the Material Point Method

Y. J. GUO[1] and J. A. NAIRN[2]
1. Material Science & Engineering, University of Utah, Salt Lake City, Utah 84112, USA
2. Wood Science & Engineering, Oregon State University, Corvallis, OR, 97331, USA

Abstract: This paper describes algorithms for three-dimensional dynamic stress and fracture analysis using the material point method (MPM). By allowing dual velocity fields at background grid nodes, the method provides exact numerical implementation of explicit cracks in a predominantly meshless method. Crack contact schemes were included for automatically preventing crack surfaces from interpenetration. Crack-tip parameters, dynamic J-integral vector and mode I, II, and III stress intensity factors, were calculated from the dynamic stress solution. Comparisons to finite difference method (FDM), finite element method (FEM), and boundary element method (BEM), as well as to static theories showed that MPM can efficiently and accurately solve three-dimensional dynamic fracture problems. Since the crack description is independent of the object description, MPM could be useful for simulation of three-dimensional dynamic crack propagation in arbitrary directions.

keyword: Material point method, MPM. three-dimensional dynamic fracture, cracks, dynamic J-integral, dynamic stress intensity, contact, mode I, mode II, mode III.

1 Introduction

Because of the difficulties in experimentally measuring high-order physical quantities, such as dynamic J-integral and stress intensity factors, during fast dynamic fracture events, computational techniques are receiving considerable attention. Computer simulation of dynamic fracture is one approach to extracting detailed information for physical quantities of a dynamic crack front at any instant of time along a highly transient history of fracture. Computer simulations may be the only possible method for extracting physical quantities as a function of position along a complicated (non-planar), three-dimensional crack front. Therefore, the advancement of three-dimensional, dynamic fracture mechanics relies heavily on advancements in numerical techniques.

An early application of numerical methods to dynamic fracture problems was the finite difference method [Chen and Wilkens (1977)]. Later, the finite element method (FEM) became the preferred numerical tool due to a series of efforts made by Nishioka *et al.* [Nishioka and Atluri (1983), Nishioka (1983), Nishioka (1995), Nishioka (1997), Nishioka, Murakami, and Takemoto (1990), Nishioka (2005)]. FEM, however, has problems coping with crack propagation whenever the crack may not propagate along mesh lines. One approach is to implement moving mesh methods [Nishioka, Murakami, and Takemoto (1990), Nishioka, Tokudome, and Kinoshita (2001)] or to remesh the material object. Although such methods are able to simulate dynamic crack propagation, the computational efficiency is impacted especially for three-dimensional problems. This difficulty is one reason why true three-dimensional effects in dynamic crack propagation is a relatively un-explored area [Nishioka and Stan (2003)]. An alternative to FEM is to use meshless methods [Belytschko, Lu, and Gu (1994), Organ, Fleming, and Belytschko (1996), Batra and Ching (2002), Chen and Chen (2005), Sladek, Sladek, Krivacek, and Zhang (2005)] that have advantages dealing with arbitrary crack propagation. Although such methods handle crack propagation better than FEM, they have trouble accurately dealing with explicit cracks [Nairn (2003); Guo and Nairn (2004)] and have not dealt with three-dimensional crack problems.

The material point method (MPM) was introduced as a numerical method to solve problems in dynamic solid mechanics [Sulsky, Chen, and Schreyer (1994); Sulsky and Schreyer (1996); Sulsky, Zhou, and Schreyer (1995); Zhou (1998)]. In MPM, a solid body is discretized into a collection of material points (particles) with all the physical properties such as mass, volume, position, velocity, and stress. As the dynamic analysis proceeds, the phys-

ical properties are interpolated onto a background grid. The equations of motion are solved on the grid, and the grid variables advanced. The advanced grid solutions are interpolated back to update the particle properties. Due to the meshless features of the object discretization, MPM may have advantages over FEM for modeling of crack propagation because there is no need for cracks to follow grid lines. In MPM, the background grid is only used as a tool to solve the equations of motion, and not used to describe the object or the crack [Nairn (2003)]. In other words, the crack is not constrained by grid lines and is free to be oriented and to propagate in any direction.

Conventional MPM, however, is not capable of handling explicit cracks due to the nature of a single velocity field on the background. Recently, conventional MPM was extended by introducing multiple nodal velocity fields to solve two-dimensional dynamic crack problems [Nairn (2003); Guo and Nairn (2004)]. The multiple velocity fields represent velocities above and below cracks that enable representation of discontinuities, such as displacement discontinuities, which are necessary for description of explicit cracks. This paper extends the two-dimensional dynamic fracture algorithms [Nairn (2003); Guo and Nairn (2004)] to three dimensional cracks and three-dimensional crack-front parameter calculations.

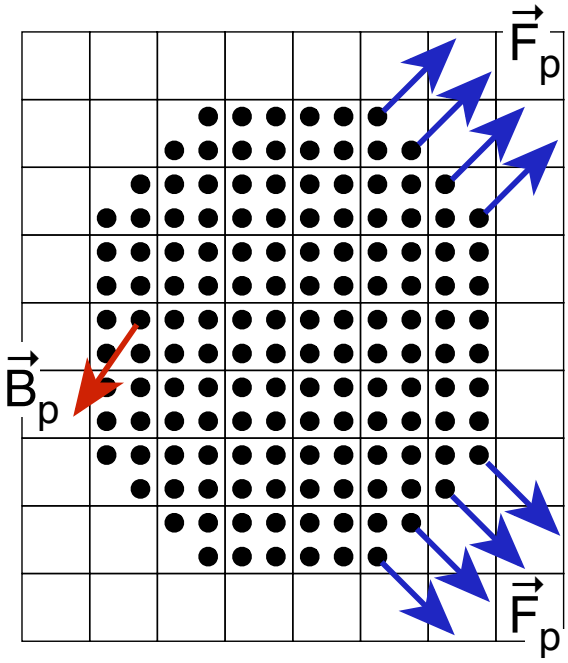

Figure 1 : Discretization of a material body into material points with applied forces and body forces on a background grid in conventional MPM.

2 MPM Algorithm with Explicit Cracks

2.1 Conventional Material Point Method

First consider a solid body without cracks subjected to volume forces, $\vec{B}$, and surface forces, $\vec{T}$, as shown in fig. 1. The problem is discretized by introducing a background grid and describing the object with a collection of material points. By the usual MPM methods [Sulsky, Chen, and Schreyer (1994)], the equations of motion for nodal momenta ($\vec{P}_i$) or nodal accelerations ($\vec{a}_i$) are

$$\frac{d\vec{P}_i}{dt} = M_i^L \vec{a}_i = \vec{f}_i^{ext} + \vec{f}_i^{int} = \vec{f}_i^{tot} \tag{1}$$

where M_i^L is the nodal mass and f_i^{ext} and f_i^{int} are nodal forces given by

$$M_i^L = \sum_p m_p N_i(\vec{x}_p) \tag{2}$$

$$\vec{f}_i^{ext} = \sum_p \left(m_p \vec{B}_p + \vec{F}_p - k\vec{v}_p \right) N_i(\vec{x}_p) \tag{3}$$

$$\vec{f}_i^{int} = -\sum_p m_p \sigma_p \cdot \nabla N_i(\vec{x}_p) \tag{4}$$

The sums are over the particles, m_p is particle mass, $\vec{B}_p$ is body force on each particle, $\vec{F}_p$ is an external particle force used to represent traction loads on the surfaces, k is an external damping coefficient that can be used to drive dynamic problems to a static limit, $\vec{v}_p$ is particle velocity, and σ_p is particle stress. $N_i(\vec{x}_p)$ and $\nabla N_i(\vec{x}_p)$ are shape functions and shape function gradients associated with node i at the position of particle p. When damping was used, k was varied until oscillations damped in a few cycles. The specific value of k has little meaning and depends on problem size, loading conditions, geometry, *etc.*.

On each explicit time step of time Δt, the nodal momenta are updated using

$$\vec{P}_i^* = \vec{P}_i + \vec{f}_i^{tot} \Delta t \tag{5}$$

The nodal accelerations ($\vec{a}_i = \vec{f}_i^{tot} / M_i^L$) and updated nodal velocities ($\vec{v}_i^* = \vec{P}_i^* / M_i^L$) are then used to update the particle velocity ($\vec{v}_p$), position ($\vec{x}_p$) and strain tensor

(ε_p), as follows:

$$\vec{v}_p^* = \vec{v}_p + \Delta t \sum_i \vec{a}_i N_i(\vec{x}_p) \quad (6)$$

$$\vec{x}_p^* = \vec{x}_p + \Delta t \sum_i \vec{v}_i^* N_i(\vec{x}_p) \quad (7)$$

$$\varepsilon_{p,mn}^* = \varepsilon_{p,mn} + \frac{\Delta t}{2}\left(\frac{\partial v_{p,m}}{\partial x_n} + \frac{\partial v_{p,n}}{\partial x_m}\right) \quad (m,n = 1,2,3) \quad (8)$$

where $\partial v_{p,m}/\partial x_n$ denote the velocity gradients of the particles, evaluated by

$$\frac{\partial v_{p,m}}{\partial x_n} = \sum_i v_{i,m} \frac{\partial N_i(\vec{x}_p)}{\partial x_n} \quad (9)$$

Once the strain or velocity gradient increments on the particles are determined, the stress increment of the particles can be determined by any implemented constitutive law for the material. Notice that Eq. (8) updates the strain using particle velocities at the start of the time step rather than using the updated particle velocities [Bardenhagen (2002)]. The initial MPM algorithm [Sulsky, Chen, and Schreyer (1994)] updated strain using $\vec{v}_p^*$, but frequently gave poor results. The initial algorithm has been replaced by updating strain as in Eq. (8), by a modified approach that updates strain after particle velocity updating [Sulsky, Zhou, and Schreyer (1995)], or by a combination of these two approaches [Nairn (2003)]. The calculations in this paper used the update based on initial velocities.

2.2 *Cracks in the Material Point Method (CRAMP)*

The previous section gave the algorithms for conventional MPM analysis when there are no cracks. In conventional MPM, the background grid describes a single velocity field, which makes it impossible to record discontinuous velocity fields that occur at cracks. The essential difference of MPM with explicit cracks and conventional MPM is that the background grid has dual nodal velocity fields, which are used to record the properties of the particles above and below the cracks, respectively [Nairn (2003); Guo and Nairn (2004)]. The extension of MPM to have explicit cracks has been termed CRAMP for CRAcks in MPM [Nairn (2003)]. Each time step of a CRAMP analysis includes the following tasks:

a. *Determine the velocity field of each particle-node pair*: The first step in CRAMP is to detect the velocity field for each particle-node pair (with non-zero shape function or with p and i such that $N_i(\vec{x}_p) \neq 0$), denoted by

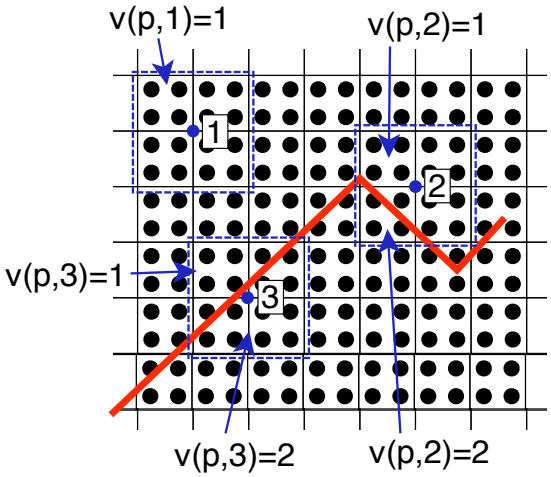

Figure 2 : Velocity fields of the particle-node pairs when the node is in crack and non-crack zones: (1) node in a non-crack zone (both the node and the particles around it are in the same side of the crack); (2) node in crack-zone and above the crack; (3) node in crack-zone and below the crack.

$\nu(p,i) = 1$ or 2. Here 1 denotes either a particle-node pair remote from all cracks (such as the particles around node 1 in fig. 2) or a particle-node pair near a crack but with the particle above the crack (such as the particles around nodes 2 and 3 in fig. 2 and above the crack). $\nu(p,i) = 2$ denotes a particle-node pair near a crack but with the particle below the crack (such as the particles around nodes 2 and 3 in fig. 2 and below the crack). A node is near a crack if a connecting line from that node to any particle surrounding the node (with non-zero shape function) crosses the crack surface. In three-dimensional MPM analysis with cracks, the crack surface is discretized into a set of triangular elements, and the crack front is represented by a set of spatial line segments, as shown in Figure fig. 3a. The detailed algorithms to determine the velocity fields are given in Appendix A. The determination of velocity fields is the most time-consuming additional calculation in CRAMP, especially for three-dimensional problems; it must be done efficiently.

The above step refers to a single crack. The algorithm is trivially extended to any number of cracks provided velocity fields at each node can be associated with a single crack. Dealing with interacting cracks or with crack branching is possible, but requires dealing with the possibility of more than two velocity fields at nodes near multiple cracks or with increasing the resolution to resolve

the two cracks without needing interacting nodes.

b. *Interpolate particle properties onto the grid and solve the equations of motion*: Once the velocity fields are known, the particle properties (mass and momentum) are interpolated to the nodes, obtaining the nodal values for the two velocity fields:

$$\vec{v}_{i,k} = \frac{\vec{P}_{i,k}}{M^L_{i,k}} \qquad k = 1,2 \tag{10}$$

where $\vec{P}_{i,k}$ and $M^L_{i,k}$ are the nodal momenta and mass for velocity field k calculated with

$$M^L_{i,k} = \sum_p m_p N_i(\vec{x}_p)\delta_{k,\nu(p,i)} \tag{11}$$

$$\vec{P}_{i,k} = \sum_p m_p \vec{v}_p N_i(\vec{x}_p)\delta_{k,\nu(p,i)} \tag{12}$$

where $\delta_{k,\nu(p,i)}$ is the Kronecker delta. Similarly, the nodal forces are

$$\vec{f}^{ext}_{i,k} = \sum_p \left(m_p \vec{B}_p + \vec{F}_p - k\vec{v}_p \right) N_i(\vec{x}_p)\delta_{k,\nu(p,i)} \tag{13}$$

$$\vec{f}^{int}_{i,k} = -\sum_p m_p \sigma_p \cdot \nabla N_i(\vec{x}_p)\delta_{k,\nu(p,i)} \tag{14}$$

The initial equations of motion at each node are:

$$\frac{d\vec{P}_{i,k}}{dt} = \vec{f}^{ext}_{i,k} + \vec{f}^{int}_{i,k} \tag{15}$$

Remote from cracks, all nodes have a single velocity field assigned to $\nu(p,i) = 1$; the $k = 1$ equations for these nodes reduce to conventional MPM. Near cracks there will be two velocity fields. When these two fields are updated, it is important to constrain the update to prevent overlapping of crack surfaces. We implemented contact by stick conditions or frictional sliding [Bardenhagen, Guilkey, Roessig, Brackbill, Witzel, and Foster (2001); Nairn (2003)]. The contact algorithm can be described physically as adding nodal forces, $\vec{f}^{con}_{i,k}$, to conform to the contact law. The total nodal force and momentum update become:

$$\vec{f}^{tot}_{i,k} = \vec{f}^{ext}_{i,k} + \vec{f}^{int}_{i,k} + \vec{f}^{con}_{i,k} = M^L_{i,k}\vec{a}_{i,k} \tag{16}$$

$$\vec{P}^*_{i,k} = \vec{P}_{i,k} + \vec{f}^{tot}_{i,k}\Delta t \tag{17}$$

The contact forces are described in Appendix B.

c. *Update the properties of the particles*: The position and velocity of the particles are updated using the nodal accelerations ($\vec{a}_{i,k} = \vec{f}^{tot}_{i,k}/M^L_{i,k}$) and advanced nodal velocities ($\vec{v}^*_{i,k} = \vec{P}^*_{i,k}/M^L_{i,k}$) for the appropriate velocity field:

$$\vec{v}^*_p = \vec{v}_p + \Delta t \sum_i \vec{a}_{i,\nu(p,i)} N_i(\vec{x}_p) \tag{18}$$

$$\vec{x}^*_p = \vec{x}_p + \Delta t \sum_i \vec{v}^*_{i,\nu(p,i)} N_i(\vec{x}_p) \tag{19}$$

The strain update proceeds as above in Eq. (8) except the velocity gradients are found from

$$\frac{\partial v_{p,m}}{\partial x_n} = \sum_i v_{i,m,\nu(p,i)} \frac{\partial N_i(\vec{x}_p)}{\partial x_n} \tag{20}$$

where $v_{i,m,k}$ denotes the m^{th} component of the k^{th} velocity field on node i. Once the strain or velocity gradient increments are known on the particles, the stress increment on the particles can be determined by any implemented constitutive law for the material, exactly as in conventional MPM.

d. *Move the crack surface*: In MPM, the crack surface needs to be updated to translate along with the deforming body. In three-dimensional MPM analysis, the crack surface is discretized into a set of triangular elements with mass-less particles at the corners of the triangles. These elements can represent any crack surface shape, including non-planar cracks. The crack surface position updates by moving the crack particles using the updated center-of-mass nodal velocity field at the crack particle ($\vec{v}^*_{c,cm}$):

$$\vec{x}^*_c = \vec{x}_c + \vec{v}^*_{c,cm}\Delta t \tag{21}$$

where $\vec{x}_c$ is the position of a particle in the crack surface. The crack-particle velocity is extrapolated from the grid using

$$\vec{v}^*_{c,cm} = \sum_i \vec{v}^*_{i,c} N_i(\vec{x}_c) \tag{22}$$

where $\vec{v}^*_{i,c}$ is the updated center-of-mass velocity at node i:

$$\vec{v}^*_{i,c} = \frac{M^L_{i,1}\vec{v}^*_{i,1} + M^L_{i,2}\vec{v}^*_{i,2}}{M^L_{i,1} + M^L_{i,2}} \tag{23}$$

3 Calculation of J-Integral and Stress Intensity Factor

For numerical fracture mechanics calculations, it is desirable to calculate J-integral and stress intensity factors at the crack tip. For 2D problems, these terms are found at the crack tip [Guo and Nairn (2004)] and only involve

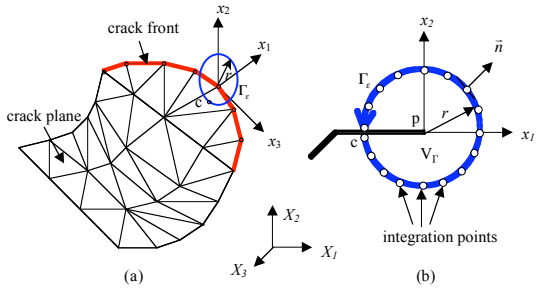

Figure 3 : 3-D crack description, crack-front coordinate system, and J-integral contour: (a) crack surface discretization. (b) J-integral contour (Γ_ε), which is a circle centered at crack tip in the x_1-x_2 plane and intersecting the crack surface at point c.

mode I and mode II stress intensity factors. For 3D problems, these terms are calculated as a function of position along the crack front and add a mode III stress intensity factor. Calculation of 3D, crack front parameters is described in this section.

3.1 Crack-Front Coordinate System

The crack front of a 3D crack is divided into a series of crack-front segments. We can simplify many operations if a transformation of the coordinate systems is performed prior to calculation of the J-integral components. Let X_1, X_2 and X_3 be a global Cartesian coordinate system; and x_1, x_2 and x_3 be the crack-front coordinate system for a particular crack-front node (see fig. 3). For the definition of a crack-front coordinate system at any point, it is sufficient to have the direction cosines for a unit vector along x_2 that is normal to the crack surface at that position:

$$\vec{\nu}_2 = \{l_2, m_2, n_2\} \tag{24}$$

and the direction cosines for a unit vector along x_3 that is tangential to the crack front and in the crack surface at that point:

$$\vec{\nu}_3 = \{l_3, m_3, n_3\} \tag{25}$$

The direction cosines of the last axis are then

$$\vec{\nu}_1 = \{l_1, m_1, n_1\} = \vec{\nu}_2 \times \vec{\nu}_3 \tag{26}$$

The transformation of coordinates, displacements, displacement gradients, and stress tensor are then:

$$x_i = \alpha_{ij} X_j \tag{27}$$
$$u_i = \alpha_{ij} u_j^g \tag{28}$$
$$u_{i,j} = \alpha_{im}\alpha_{jn} u_{m,n}^g \tag{29}$$
$$\sigma_{ij} = \alpha_{im}\alpha_{jn}\sigma_{mn}^g \tag{30}$$

where the variables with superscript g stand for the values in the global coordinate system and α_{ij} is the coordinate transformation matrix:

$$\alpha_{ij} = \begin{bmatrix} l_1 & m_1 & n_1 \\ l_2 & m_2 & n_2 \\ l_3 & m_3 & n_3 \end{bmatrix} \tag{31}$$

3.2 Dynamic J-integral Vector

The most general and useful way to predict the behavior of a cracked body is through the use of the J-integral fracture criterion. The definition of J-integral components at a crack tip in dynamic fracture analysis was derived by Nishioka and Atluri (1983) and Nishioka (1995). For each crack-front segment, the dynamic J-integral vector is defined in the crack-front local coordinates by

$$J_k = \lim_{\varepsilon\to 0}\int_{\Gamma_\varepsilon}\left[(W+K)\cdot n_k - \sigma_{ij}n_j\frac{\partial u_i}{\partial x_k}\right]d\Gamma \tag{32}$$
$$= \int_{\Gamma+\Gamma_c}\left[(W+K)\cdot n_k - \sigma_{ij}n_j\frac{\partial u_i}{\partial x_k}\right]d\Gamma + \int_{V_\Gamma}\left(\rho\ddot{u}_i u_{i,k} - \rho\dot{u}_i\dot{u}_{i,k}\right)dV \tag{33}$$

where $k = 1, 2$; W and K denote the stress-work density and kinetic energy density, respectively; σ_{ij} are stresses; u_i represent displacements (accordingly, $\partial u_i/\partial x_k$ are the components of the displacement gradient); n_k are components of the unit normal vector ($\vec{n}$) to the J-integral contour Γ_ε (see fig. 3b). Furthermore,

$$W = \int \sigma_{ij}\, d\varepsilon_{ij} \tag{34}$$
$$K = \frac{1}{2}\rho\dot{u}_i\dot{u}_i \tag{35}$$

where ρ is the mass density.

Integral paths are defined as follows: Γ is a far-field contour that encloses the crack tip and envelops a volume V_Γ; Γ_ε is a near-field contour arbitrarily close to the crack

tip and envelops an infinitesimal volume V_ε; and Γ_c is the crack surface enclosed by Γ. In practice, we usually select a near-field contour which is a circle centered at crack tip with a radius of 2 times of mesh cell size, as shown in fig. 3b. Note that the $k = 1$ component (J_1) in Eq. (33) is the total energy release rate for elastic materials.

The key terms in Eqs. (32) and (33) are known on the particles, but to calculate dynamic J-integral, they have to be extrapolated to the nodes for subsequent numerical integration. The extrapolations to the grid are

$$q_{i,k} = \frac{\sum_p m_p q_p N_i(\vec{x}_p)\delta_{k,\mathrm{v}(p,i)}}{M^L_{i,k}} \tag{36}$$

where $q_{i,k}$ is the value of the k^{th} velocity field at node i for any property q and q_p is particle value of the property. Once the nodal results are obtained, the solution at any position ($\vec{X}_p$) for either velocity field is

$$q(\vec{X}_p) = \sum_i q_{i,\mathrm{v}(p,i)} N_i(\vec{X}) \tag{37}$$

J-integral is calculated at crack-front nodes, as shown in fig. 3a. There are several steps to the task:

1. Find the intersection (point c in fig. 3a) between the J-integral contour and the crack surface;
2. Divide the J-integral contour into n_j segments. Accordingly, there are $n_j + 1$ points along the J-integral contour;
3. Find the coordinates ($\vec{x}_p$) of the points on the contour in the local crack-tip coordinates;
4. Determine the coordinates ($\vec{X}_p$) of the points in the global coordinates by coordinate transformation (Eq. (27));
5. Compute the solutions of all required, J-integral terms in Eqs. (32) and (33) at the points ($\vec{X}_p$) in the global coordinates using Eq. (37);
6. Transform the global solutions for all terms to the crack-front coordinates, getting the solutions for strain-energy density (W), kinetic-energy density (K), stresses (σ_{ij}) and displacement gradients ($\partial u_i/\partial x_j$) in the crack-tip coordinates.

Once the solutions of the variables required for J-integral calculation are determined in the crack-tip coordinates, the J-integral in the local coordinate system can be calculated by numerical integration using the midpoint rule:

$$J_k = \frac{\pi r}{n_j}\sum_{i=1}^{n_j}\left(F_k^i + F_k^{i+1}\right) \qquad k = 1,\ 2 \tag{38}$$

where summation is conducted on the segments of the J-integral contour or radius r and F_k^i denotes the value of integrand (F_k) at point i on the J-integral contour:

$$F_k = (W + K)n_k - \sigma_{ij} n_j \frac{\partial u_i}{\partial x_k} \tag{39}$$

when using Eq. (32). Numerical results showed that $n_j = 16$ was sufficient for accurate results.

3.3 Calculation of Dynamic Stress Intensity

Once the dynamic J-integral is obtained, the results can be converted to crack tip mode I, II, and III, stress intensity factors. For isotropic, linear elastic materials, the relation between the total energy release rate ($G = J_1$) and the stress intensity factors is [Nishioka (1995); Nishioka, Murakami, and Takemoto (1990)]

$$G = \frac{1}{2\mu}\left(A_I K_I^2 + A_{II} K_{II}^2 + A_{III} K_{III}^2\right) \tag{40}$$

where K_I, K_{II}, and K_{III} are the components of pure modes I, II, and III stress intensity factors. A_I, A_{II}, and A_{III} are parameters related to crack propagation velocity (C):

$$A_I = \frac{\beta_I(1-\beta_{II}^2)}{4\beta_I\beta_{II} - (1+\beta_{II}^2)^2} \tag{41}$$

$$A_{II} = \frac{\beta_{II}(1-\beta_{II}^2)}{4\beta_I\beta_{II} - (1+\beta_{II}^2)^2} \tag{42}$$

$$A_{III} = \frac{1}{\beta_{II}} \tag{43}$$

where

$$\beta_I = \sqrt{1 - \frac{C^2}{C_s^2}} \tag{44}$$

$$\beta_{II} = \sqrt{1 - \frac{C^2}{C_d^2}} \tag{45}$$

where $C_s^2 = \mu/\rho$ and $C_d^2 = (\kappa+1)\mu/((\kappa-1)\rho)$, and μ and ρ are shear modulus and density of the material. Taking

the limit as $C \to 0$ for the stationary crack calculations in this paper leads to $A_I = A_{II} = (\kappa+1)/4$, and $A_{III} = 1$. In the above equations, $\kappa = (3-\nu)/(1+\nu)$ for plane stress and $\kappa = 3-4\nu$ for plane strain, where ν is Poissons ratio.

According to linear elastic fracture mechanics, the stress intensity factors can be expressed by the crack opening displacements near the crack tip

$$\Delta u_I = \frac{2(1-\nu)}{\mu}\sqrt{\frac{R}{2\pi}}K_I \quad (46)$$

$$\Delta u_{II} = \frac{2(1-\nu)}{\mu}\sqrt{\frac{R}{2\pi}}K_{II} \quad (47)$$

$$\Delta u_{III} = \frac{2}{\mu}\sqrt{\frac{R}{2\pi}}K_{III} \quad (48)$$

where Δu_I, Δu_{II}, and Δu_{III} are the crack opening, shearing, and tearing displacements, taken in the limit as the distance R from the crack tip approaches zero. Combining Eq. (40) with the crack-tip displacements, the stress intensity factors can be found from the total energy release rate and the ratios of the crack opening displacements using

$$|K_I| = \sqrt{\frac{2\mu G}{A_I + A_{II}\gamma_{12}^2 + A_{III}\gamma_{31}^2}} \quad (49)$$

$$|K_{II}| = |\gamma_{21}K_I| \quad (50)$$

$$|K_{III}| = |\gamma_{31}K_I| \quad (51)$$

where $\gamma_{21} = \Delta u_{II}/\Delta u_I$ and $\gamma_{31} = \Delta u_{III}/\Delta u_I$. These equations assume Δu_I is non-zero. If it is zero, alternate equations can derived. If Δu_{II} is non-zero, the relations are:

$$|K_{II}| = \sqrt{\frac{2\mu G}{A_I\gamma_{12}^2 + A_{II} + A_{III}\gamma_{32}^2}} \quad (52)$$

$$|K_I| = |\gamma_{12}K_I| \quad (53)$$

$$|K_{III}| = |\gamma_{32}K_I| \quad (54)$$

where $\gamma_{12} = \Delta u_I/\Delta u_{II}$ and $\gamma_{32} = \Delta u_{III}/\Delta u_{II}$. If Δu_{III} is non-zero, the relations are:

$$|K_{III}| = \sqrt{\frac{2\mu G}{A_I\gamma_{13}^2 + A_{II}\gamma_{23}^2 + A_{III}}} \quad (55)$$

$$|K_I| = |\gamma_{13}K_I| \quad (56)$$

$$|K_{II}| = |\gamma_{23}K_I| \quad (57)$$

where $\gamma_{13} = \Delta u_I/\Delta u_{III}$ and $\gamma_{23} = \Delta u_{II}/\Delta u_{III}$. The signs of the stress intensity factors are determined by the signs of the corresponding crack tip displacements (Δu_I, Δu_{II}, and Δu_{III}).

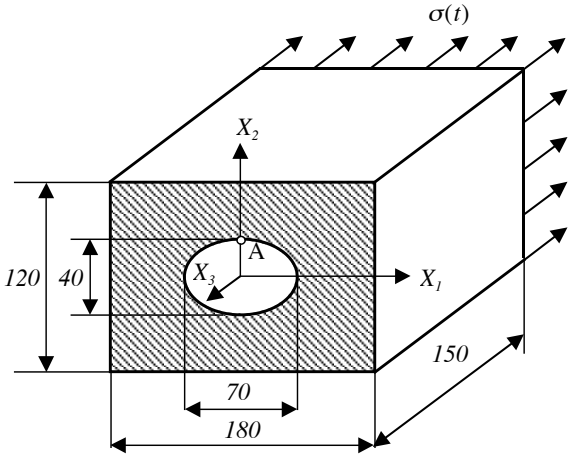

Figure 4 : Sketch of a rectangular rod (half) with an embedded elliptical crack under axial tension (dimensions in *mm*).

4 Results and Discussion

4.1 Rectangular Rod with an Embedded Elliptical Crack

To verify the above algorithms and MPM for solving three-dimensional fracture problems, a rectangular rod with an embedded elliptical crack subjected to an axial tensile load ($\sigma(t) = 400$ MPa for $t \geq 0$) was employed to calculate dynamic J-integral and stress intensity. As shown in fig. 4, the specimen was 300 mm long, 180 mm wide and 120 mm high, and loaded dynamically in the axial direction. An elliptical crack, with a major axis of 70 mm and a minor axis of 40 mm, was located centrally in the mid-plane of the specimen. Only half of the specimen along the loading direction is shown in fig. 4 to show the crack surface. The material used in the analysis was assumed to be linear elastic with shear modulus of 77 GPa and bulk modulus of 165 GPa (*i.e.*, tensile modulus of 200 GPa and Poissons ratio of 0.298). The mass density of the material was 7900 kg/m^3.

Because of the bi-axial symmetry of the specimen, only one quarter of the specimen ($X_1 \geq 0$ and $X_2 \geq 0$) was analyzed. The entire length in the X_3 direction was analyzed to make the crack an internal, explicit crack. The size of the cells in the background mesh were varied from $7.5 \times 7.5 \times 7.5$ mm to $3 \times 3 \times 3$ mm, which generated

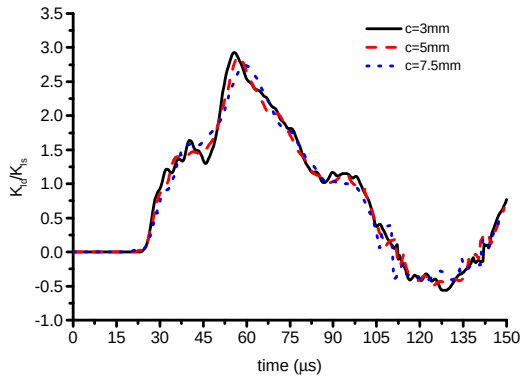

Figure 5 : Effect of mesh size on the dynamic stress intensity in a rectangular rod with an embedded elliptical crack

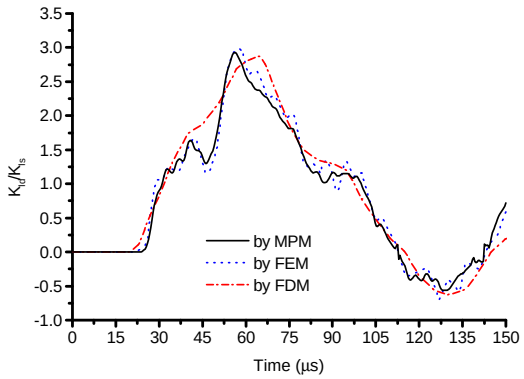

Figure 6 : Comparison of the results of the dynamic stress intensity factor evaluated by MPM, finite element method (FEM) and finite difference method (FDM) for a rectangular rod with an embedded elliptical crack.

from 30,720 to 480,000 particles in total. A reduction in cell size by linear factor f increased computational time by a factor of f^4. The power of 4 was due to each geometric dimension and the time dimension due to smaller cells requiring smaller step sizes. The crack calculations did not cause additional time increases for smaller cells. The J-integral and stress intensity factor at the deepest point (point A in fig. 4) were calculated. The J-integral contour was a circle in the X_2-X_3 plane with its center located at point A and a radius equal to two cell widths. The results for dynamic K_{Id}, normalized to the static K_{Is} of 83.6 MPa $\sqrt{\text{m}}$, for three different mesh cell sizes are given in fig. 5. These undamped calculations show the initial oscillations in dynamic stress intensity factor as the stress wave first encounters the crack tip. The results show that stress intensity factor was insensitive to the mesh sizes used and therefore converged even for relatively coarse meshes. The coarsest mesh (7.5 mm cells) had particle spacings that were 9.4% of the crack length. The results were further validated by comparison to calculations on the same specimen by other methods. Figure 6 compares MPM results to prior numerical results evaluated by the finite element (FEM) [Nishioka (1995)] and finite difference methods (FDM) [Chen and Wilkens (1977)]. The results of stress intensity evaluated by MPM agreed very well with FEM results. There was more deviation when compared to FDM, which is likely because FDM is less accurate than either FEM or MPM.

Path independence of the dynamic J-integral was evaluated at constant mesh size ($\Delta = 3$ mm mesh) while varying the radius of the path using $r = 6$, 9, or 18 mm (see circle in fig. 3b). The results for dynamic J-integral calculated by MPM using either Eq. (32) or Eq. (33) are plotted in fig. 7 and fig. 8. The results in fig. 7 show that Eq. (32), which excluded the volume integral term, is relatively insensitive to path size for this problem and the chosen path sizes, but does start to show deviations when $r = 18$ mm. In contrast, the full equation in Eq. (33) is path independent as shown in fig. 8. Provided the path is small, the dynamic J-integral can be found by the contour integral in Eq. (32), which is computationally more efficient. For larger paths, accurate path-independent results require both the contour integral and the volume integral in Eq. (33). The volume integral was evaluated numerically over the zone enclosed the the path.

4.2 Thin-Walled Cylinder with Inner-Surface Crack

The next example was a thin-walled cylinder with an elliptical crack on the inner surface. A cylinder, with radius $R = 200$ mm and thickness $t = 40$ mm, was loaded axially by a uniform tension ($\sigma(t) = 100$ MPa, $t \geq 0$). Figure 9 depicts half the cylinder with a length of $2l = 2 \times 120$ mm. A circumferential semi-elliptical crack was located at the inner surface of the cell as shown in fig. 9, where points A, B, and C are on the minor and major axes of the elliptical crack. The semi-elliptical crack was assumed to have a major axis of $\overline{BC} = 80$ mm

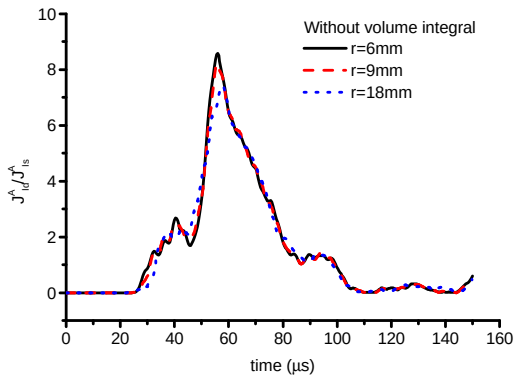

Figure 7 : Effect of the size of the contour on the J-integral when calculated without the volume integral, *i.e.*, when using Eq. (32).

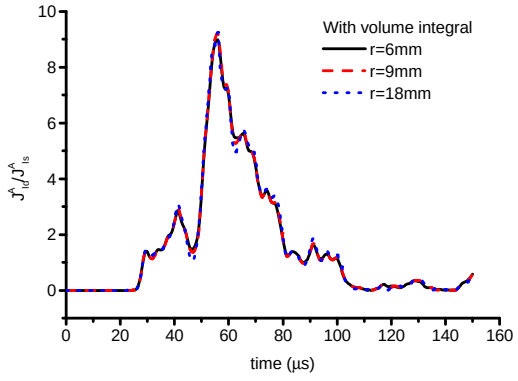

Figure 8 : Effect of the size of the contour on the J-integral when calculated with the volume integral, *i.e.*, when using Eq. (33).

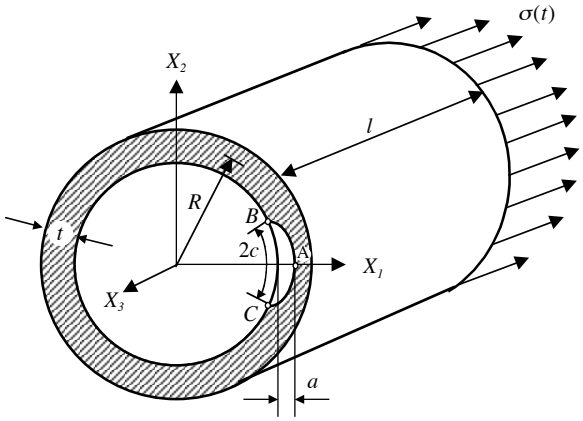

Figure 9 : Sketch of a thin-walled cylinder (half of the specimen) with an elliptical crack on the inner surface and loded in tension.

($2c = 80.676$ mm) and a depth of $a = 21$ mm from the inner surface. Due to symmetry, only half ($X_2 \geq 0$) of the cylinder cell was analyzed, and the displacement boundary conditions on the plane of $X_2 = 0$ were thus set to $u_2 = 0$. The entire length in the X_3 direction was analyzed to make the crack an internal, explicit crack. The material properties were the same as in the previous example. The cell size for background mesh was $3 \times 5 \times 5$ mm, which generated a total of 643,584 particles. The non-cubical grid was used to add resolution in the X_1 direction for better resolution of the crack. Such grids are fine in MPM.

The dynamic stress intensity at the deepest location (point A in fig. 9) of the crack was calculated using a circular contour in the X_1-X_3 plane with the center located at point A and a radius of 10 mm. The dynamic stress intensity is plotted in fig. 10, where the dynamic stress intensity was normalized by the static stress intensity result [Anderson (1995)]:

$$K_{Is} = \sigma \sqrt{\frac{\pi a}{Q}} F_t \tag{58}$$

where σ is the applied stress. Quantities Q and F_t are

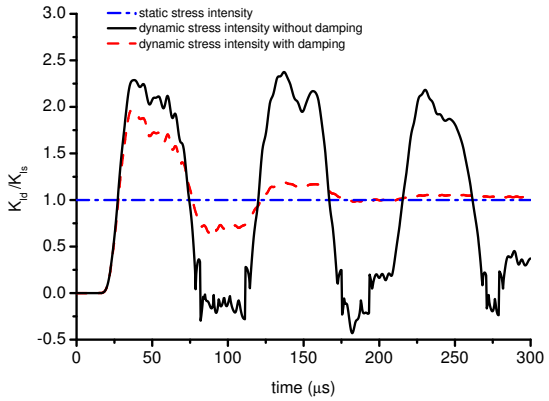

Figure 10 : Dynamic stress intensity evaluated by MPM for a thin-walled cylinder with an elliptical crack on the inner surface under axial tension.

given by

$$Q = 1+1.464\left(\frac{a}{c}\right)^{1.65} \tag{59}$$

$$F_t = 1+\left[0.02+\xi(0.0103+0.00617\xi) +0.0035(1+0.7\xi)\left(\frac{R}{t}-5\right)^{0.7}\right]Q^2 \tag{60}$$

where $\xi = 2c/t$. Note that the formula (Eq. (58)) for the static stress intensity is only valid for thin cylinders with $R/t \geq 5$; the MPM calculations had $R/t = 5$. For these calculations $K_{Is} = 24.1$ MPa $\sqrt{\text{m}}$.

As seen in fig. 10, the dynamic stress intensity without damping vibrates with an average value approximately equal to the static stress intensity factor (K_{Is}). With the addition of damping, the dynamic stress intensity converged to the static value at long times.

4.3 Cylindrical Bar with an Inclined Crack

For a 3D, mixed-mode stress intensity example, a cylindrical bar with an inclined penny-shaped crack was selected, as shown in fig. 11. The specimen was subjected to a step loading ($\sigma(t) = 40$ MPa, $t \geq 0$). The modulus and Poisson ratio of the material were set to $E = 2$ GPa and $\nu = 0.298$. The angle between the crack surface and loading direction was 60°. The length and radius of the cylindrical bar were 100 mm, and 50 mm, respectively. The mesh size used was $2\times2\times2$ mm, and the radius of

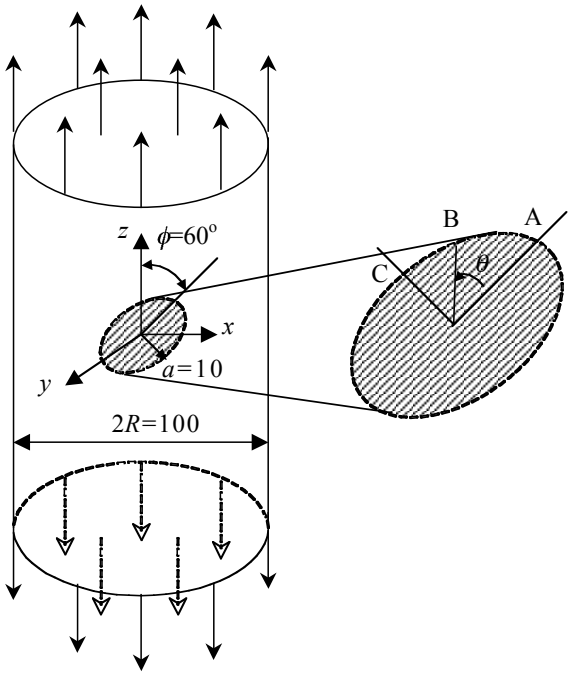

Figure 11 : Sketch of a cylindrical bar with an inclined penny-shaped crack under axial tension.

J-integral path was 4 mm, *i.e.*, twice the cell size. In order to compare the MPM results with the static theoretical results, artificial damping was added to the MPM calculations. The static theoretical results are incorporated in the figures for comparison, which are [Tada, Paris, and Irwin (2000)]:

$$K_I^s = \frac{2}{\pi}\sigma\sqrt{\pi a}\cos^2\alpha \tag{61}$$

$$K_{II}^s = \frac{4}{\pi(2-\nu)}\sigma\sqrt{\pi a}\cos\alpha\sin\alpha\cos\theta \tag{62}$$

$$K_{III}^s = \frac{4(1-\nu)}{\pi(2-\nu)}\sigma\sqrt{\pi a}\cos\alpha\sin\alpha\sin\theta \tag{63}$$

where $\alpha = 90^\circ - \phi$.

The results for dynamic stress intensity in modes *I*, *II*, and *III* at points *A* (where $\theta = 0^\circ$), *B* (where $\theta = 45^\circ$, and *C* (where $\theta = 90^\circ$) are plotted in figs. 12, 13, and 14. All stress intensity factors were normalized by

$$K_0 = \frac{2}{\pi}\sigma\sqrt{\pi a} \tag{64}$$

All three dynamic stress intensity factors, with damping, converged to the static theoretical results at long times.

The MPM results for normalized stress intensity factors along the crack front from $\theta = 0^\circ$ to 90° at time

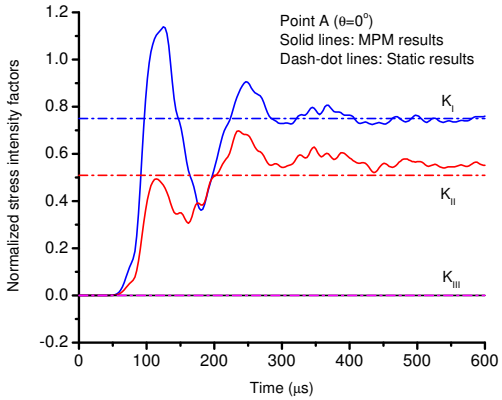

Figure 12 : Mode *I*, *II*, and *III* stress intensity factors at point *A* on the edge of an inclined penny-shaped crack under axial tension calculated by MPM with damping.

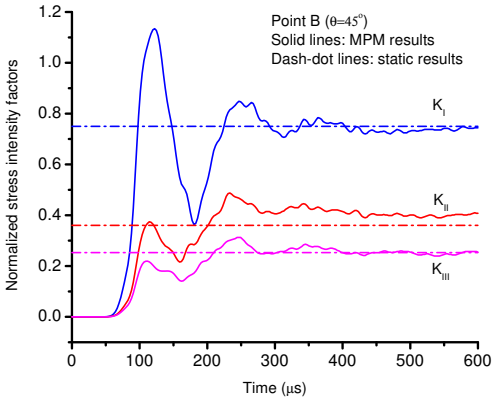

Figure 13 : Mode *I*, *II*, and *III* stress intensity factors at point *B* on the edge of an inclined penny-shaped crack under axial tension calculated by MPM with damping.

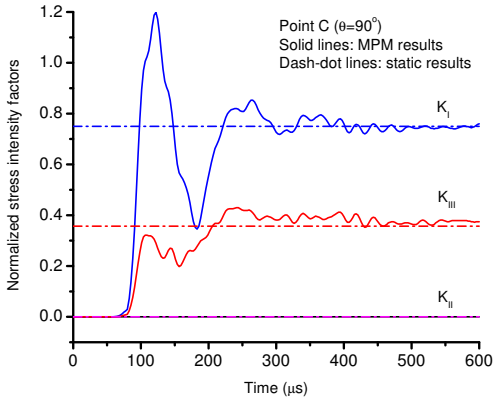

Figure 14 : Mode *I*, *II*, and *III* stress intensity factors at point *C* on the edge of an inclined penny-shaped crack under axial tension calculated by MPM with damping.

$t = 600$ μs, which corresponds to convergence to the static results, are compared with the normalized, analytical, static stress intensity factors in fig. 15. The MPM results agreed well with the static theoretical results.

5 Conclusions

This paper describes algorithms for crack-tip fracture parameters for three-dimensional dynamic problems with explicit cracks using the meshless material point method (MPM). The results for *J*-integral and stress intensity factors evaluated by MPM were compared with the results generated by other approaches, including finite element method (FEM), finite difference method (FDM), dynamic boundary element method (BEM), as well as static theories. The comparisons showed that MPM is a reliable approach for conducting dynamic stress and fracture analysis with high computational accuracy and efficiency. Since the crack surface is an independent entity in MPM analysis, not connected to the mesh, there is no need to re-mesh the problem during simulations of 3D crack propagation. It is reasonable to expect that MPM will be a useful tool in the simulation of three-dimensional crack propagation.

Acknowledgement: This work was supported by a grant from the Department of Energy DE-FG03-02ER45914 and by the University of Utah Center for the Simulation of Accidental Fires and Explosions (C-SAFE), funded by the Department of Energy,

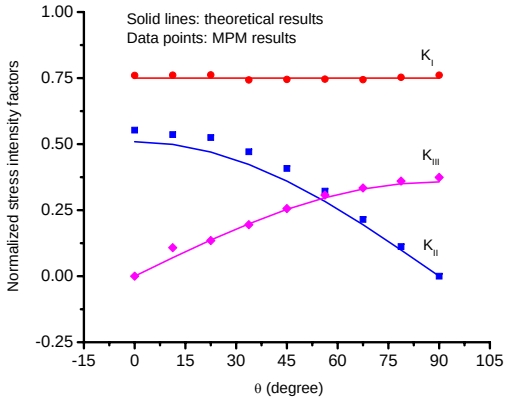

Figure 15 : Mode *I*, *II*, and *III* stress intensity factors in the static limit as a function of position along the crack front compared to analytical results.

Lawrence Livermore National Laboratory, under Subcontract B341493.

References

Anderson, T. L. (1995): *Fracture Mechanics: Fundamentals and Applications*. CRC press, Boca Raton, FL, second edition.

Bardenhagen, S. G. (2002): Energy conservation error in the material point method. *J. Comp. Phys.*, vol. 180, pp. 383–403.

Bardenhagen, S. G.; Brackbill, J. U.; Sulsky, D. (2000): The material point method for granular materials. *Computer Methods in Applied Mechanics and Engineering*, vol. 187, pp. 529–541.

Bardenhagen, S. G.; Guilkey, J. E.; Roessig, K. M.; Brackbill, J. U.; Witzel, W. M.; Foster, J. C. (2001): An improved contact algorithm for the material point method and application to stress propagation in granular material. *Computer Modeling in Engineering & Sciences*, vol. 2, pp. 509–522.

Batra, R. C.; Ching, H.-K. (2002): Analysis of elastodynamic deformations near a crack/notch tip by the meshless local Petrov- Galerkin (MLPG) method. *Computer Modeling in Engineering & Sciences*, vol. 3, pp. 717–730.

Belytschko, T.; Lu, Y. Y.; Gu, L. (1994): Element-free Galerkin methods. *Int. J. Num. Meth. Engrg.*, vol. 37, pp. 229–256.

Chen, W.-H.; Chen, C.-H. (2005): On three-dimensional fracture mechanics analysis by an enriched meshless method. *Computer Modeling in Engineering & Sciences*, vol. 8, no. 3, pp. 177–190.

Chen, Y. M.; Wilkens, M. L. (1977): *Numerical Analysis of Dynamic Crack Problems*, pp. 317–325. In *Elastodynamic Crack Problems*, Noordhoff International Publishing, The Netherlands, 1977.

Guo, Y.; Nairn, J. A. (2004): Calculation of J-integral and stress intensity factors using the material point method. *Computer Modeling in Engineering & Sciences*, vol. 6, pp. 295–308.

Nairn, J. A. (2003): Material point method calculations with explicit cracks. *Computer Modeling in Engineering & Sciences*, vol. 4, pp. 649–664.

Nairn, J. A. (2006): On the calculation of energy release rates for cracked laminates with residual stresses. *Int. J Fract. Mech.*, vol. 139, no. 267–293.

Nishioka, T. (1983): A numerical study of the use of path independent integrals in elastic-dynamic crack propagation. *Engr. Fract. Mech.*, vol. 18, pp. 23–33.

Nishioka, T. (1995): *Recent Developments in Computational Dynamic Fracture Mechanics*, pp. 1–58. In *Dynamic Fracture Mechanics*, Computational Mechanics Publications, Southampton, UK, 1995.

Nishioka, T. (1997): Computational dynamic fracture mechanics. *Int. J. Fract.*, vol. 86, pp. 127–159.

Nishioka, T. (2005): Recent advances in numerical simulation technologies for various dynamic fracture phenomena. *Computer Modeling in Engineering & Sciences*, vol. 10, no. 3, pp. 209–216.

Nishioka, T.; Atluri, S. N. (1983): Path-independent integrals, energy release rates, and general solutions of near-tip fields in mixed-mode dynamic fracture mechanics. *Engr. Fract. Mech.*, vol. 18, pp. 1–22.

Nishioka, T.; Murakami, R.; Takemoto, Y. (1990): The use of the dynamic J jntegral (J') in finite-element simulation of mode I and mixed-mode dynamic crack

propagation. *International Journal of Pressure Vessels and Piping*, vol. 44, pp. 329–352.

Nishioka, T.; Stan, F. (2003): A hybrid experimental-numerical study on the mechanism of three-dimensional dynamic fracture. *Computer Modeling in Engineering & Sciences*, vol. 4, pp. 119–140.

Nishioka, T.; Tokudome, H.; Kinoshita, M. (2001): Dynamic fracture-path prediction in impact fracture phenomena using moving finite element method based on delaunay automatic mesh generation. *Int. J. Solids Struct.*, vol. 38, pp. 5273–5301.

Organ, D. J.; Fleming, M.; Belytschko, T. (1996): Continuous meshless approximations for nonconvex bodies by diffraction and transparency. *Computational Mechanics*, vol. 18, pp. 225–235.

Sladek, J.; Sladek, V.; Krivacek, J.; Zhang, C. (2005): Meshless local petrov-galerkin method for stress and crack analysis in 3-d axisymmetric fgm bodies. *Computer Modeling in Engineering & Sciences*, vol. 8, no. 3, pp. 259–270.

Sulsky, D.; Chen, Z.; Schreyer, H. L. (1994): A particle method for history-dependent materials. *Comput. Methods Appl. Mech. Engrg.*, vol. 118, pp. 179–186.

Sulsky, D.; Schreyer, H. K. (1996): Axisymnmetric form of the material point method with applications to upsetting and Taylor impact problems. *Comput. Methods. Appl. Mech. Engrg*, vol. 139, pp. 409–429.

Sulsky, D.; Zhou, S.-J.; Schreyer, H. L. (1995): Application of a particle-in-cell method to solid mechanics. *Comput. Phys. Commun.*, vol. 87, pp. 236–252.

Tada, H.; Paris, P. C.; Irwin, G. (2000): *The Stress Analysis of Cracks Handbook: Third Edition*. ASM International.

Zhou, S. (1998): *The Numerical Prediction of Material Failure Based on the Material Point Method*. PhD thesis, University of New Mexico, 1998.

Appendix A: Determination of Velocity Fields

In CRAMP or MPM with cracks, the first task is to determine the velocity field of each particle-node pair. Figure 2 illustrates a material body with a crack, and the material body has been discretized into a collection of material points (particles). If all the particles with non-zero shape function around a node are on the same side of the crack, that node is in a non-crack zone (see node 1 in fig. 2). Otherwise, the node is in crack zone (see nodes 2 and 3 in fig. 2). In a typical MPM analysis, most nodes will be in non-crack zones, except for the few nodes around crack surfaces. For any node i in a non-crack zone, the velocity field of any particle is set to $\nu(p,i) = 1$. For a node in a crack zone, the particles around it with non-zero shape function are either above the crack or below the crack. If a particle around the node is above the crack, the velocity field of the particle-node pair is set to $\nu(p,i) = 1$, otherwise it is set to $\nu(p,i) = 2$.

For each particle-node pair possibly near a crack, the key task is to determine if the particle is above or below the crack or on the same side of the crack as the node. Let $\lambda(p,i)$ denote the particle-node-crack relation. It is determined by drawing a line from particle p to node i followed by

$$\lambda(p,i) = \begin{cases} 0 & \text{if line does not cross the crack} \\ 1 & \text{if line crosses the crack from above} \\ 2 & \text{if line crosses the crack from below} \end{cases} \tag{65}$$

The determination of $\lambda(p,i)$ is based on calculation of the signed volume of specific tetrahedra, given by:

$$V(A,B,C,D) = -\frac{1}{6}\begin{vmatrix} x_A & y_A & z_A & 1 \\ x_B & y_B & z_B & 1 \\ x_C & y_C & z_C & 1 \\ x_D & y_D & z_D & 1 \end{vmatrix} \tag{66}$$

where points A, B, C denote the three vertices of a triangle, and point D is an arbitrary point. The volume is positive if point D is in the direction of the outward normal of the plane (A,B,C), otherwise it is negative.

In 3D CRAMP, the crack surface is discretized into a collection of triangular elements, as shown in fig. 3a. Determination of particle-node crossing of the crack surface is done be an element by element search of the crack surface elements. For a specific crack element (see fig. 16), we define the following five volumes according to Eq. (66):

$$\begin{array}{ll} V_1 = V(1,2,3,p) & V_2 = V(1,2,3,i) \\ V_3 = V(i,1,2,p) & V_4 = V(i,1,3,p) \\ V_5 = V(i,2,3,p) & \end{array} \tag{67}$$

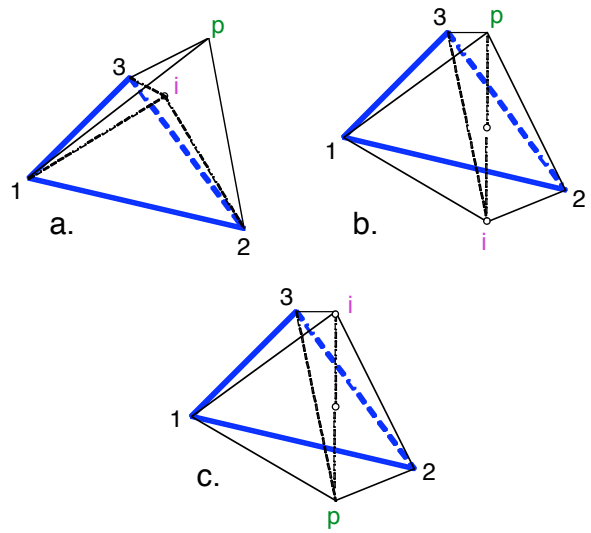

Figure 16 : Illustration of the tetrahedra used to determine velocity field of a particle-node pair, where p denotes a particle, i represents a node, and triangle 123 is a crack surface element: (a) the particle and node are in the same side or the crack ($\lambda(p,i)=0$); (b) the particle-node line segment crosses the crack surface element from above ($\lambda(p,i)=1$); (c) the particle-node line segment crosses the crack surface element from below ($\lambda(p,i)=2$).

where points 1, 2, 3 are the three vertices of a crack surface element, and points p and i denote the particle and the node, respectively. By inspection, it was determined that, $\lambda(p,i)=1$ if $V_1>0$, $V_2\le 0$, $V_3\ge 0$, $V_4\le 0$, and $V_5\ge 0$; $\lambda(p,i)=2$ if $V_1<0$, $V_2\ge 0$, $V_3\le 0$, $V_4\ge 0$, and $V_5\le 0$; and $\lambda(p,i)=0$ for all other cases. For cases 1 and 2, the first two conditions assure that the particle and node are on opposite sides; the latter three conditions specify that the particle-node line crosses the crack surface within the region of the crack element. Note that particles should never be on the crack surface whenever contact is handled correctly; therefore $V_1\neq 0$. A node, however, may be on a crack surface without disturbing the analysis. One complication in determining $\lambda(p,i)$ is that the particle-node line might cross more than one element of a single crack. In this situation, the crossing is ignored unless there are an odd number of crossings. To consider this possibility, the above steps must check all crack surface elements of a crack before deciding if there is a crossing.

Finally, $\lambda(p,i)$ is converted to the velocity field $\nu(p,i)$ for each particle-node pair, *i.e.*, $\nu(p,i)=1$ if $\lambda(p,i)=1$ or $\lambda(p,i)=0$ and $n_{i,2}\neq 0$ and $\nu(p,i)=2$ if $\lambda(p,i)=2$ or $\lambda(p,i)=0$ and $n_{i,1}\neq 0$. Here $n_{i,k}$ $(k=1,2)$ denote the number of particles around the node with non-zero shape function and $\lambda(p,i)=k$. Note that the only conversion is to decide whether $\lambda(p,i)=0$ should be $\nu(p,i)=1$ or $\nu(p,i)=2$.

Appendix B: Crack Surface Contact

Whenever a new nodal velocity field and/or acceleration field is generated, the dual-field node must be checked for crack surface contact to prevent crack surfaces from interpenetration, which is physically not allowed. In a prior paper on 2D cracks [Nairn (2003)], contact was detected by calculation of nodal volumes relative to nodal volumes for the undeformed body. During extensions to 3D, it was determined that an alternate approach based on nodal displacement is both simpler and more robust; *i.e.*, does not depend on pre-selected critical values for contact. In the displacement method, the nodal displacements are calculated by interpolating the particle displacements ($\vec{u}_p$); *i.e.*,

$$\vec{u}_{i,k}=\frac{\sum_p m_p\vec{u}_p N_{p,i}\delta_{k,\nu(p,i)}}{M^L_{i,k}} \tag{68}$$

where $k=1$ or 2 corresponds to the velocity field $\nu(p,i)=1$ or 2 or to displacements above and below the crack. The crack surfaces are assumed to be in contact if normal direction displacements overlap or if

$$(\vec{u}_{i,1}-\vec{u}_{i,2})\cdot\hat{n}_i<0 \tag{69}$$

where $\hat{n}_i$ is the normal of the crack surface near node i pointing into the material above the crack. The displacement criterion is based on zero relative displacement corresponding to closed cracks. This condition is guaranteed for all cracks in this paper which start with closed cracks prior to application of load. The approach requires modification for cracks that are initially opened.

A variant of the displacement criterion is to also check relative velocities of the crack surfaces as done previously by Bardenhagen *et al.* [Bardenhagen, Guilkey, Roessig, Brackbill, Witzel, and Foster (2001); Bardenhagen, Brackbill, and Sulsky (2000)]. The crack surfaces are moving apart if

$$(\vec{v}_{i,1}-\vec{v}_{i,2})\cdot\hat{n}_i>0 \tag{70}$$

where $\vec{v}_{i,1}$ and $\vec{v}_{i,2}$ are the nodal velocities for the particles above and below the crack. In the variant of the displacement scheme, the relative velocities are checked first. If the surfaces are moving apart, the cracks are assumed to not be in contact and the natural movement occurs. If the cracks are moving towards each other, the displacement criterion above is used to determine whether or not there is contact. It most calculations, the velocity check is superfluous, but it some problems involving friction it was found to improve accuracy. None of the problems in this paper involved friction and thus all were based solely on the displacement criterion.

Once contact is detected, a force is applied to the node to conform to a contact law. The contact laws were applied following Bardenhagen *et al.* [Bardenhagen, Guilkey, Roessig, Brackbill, Witzel, and Foster (2001); Bardenhagen, Brackbill, and Sulsky (2000)]. The only difference being that normal vector was calculated from the crack surface rather than the gradient of the mass matrix. Since there is a single normal vector, the crack contact scheme exactly conserves momentum. Two contact laws were implemented — stick and frictional sliding. In stick conditions, forces normal and tangential to the crack surface are applied above the crack at node i of

$$f_{i,N} = -\frac{M^L_{i,1}}{\Delta t}(\vec{v}_{i,1} - \vec{v}_{i,c}) \cdot \hat{n}_i \tag{71}$$

$$f_{i,T} = -\frac{M^L_{i,1}}{\Delta t}(\vec{v}_{i,1} - \vec{v}_{i,c}) \cdot \hat{t}_i \tag{72}$$

where $M^L_{i,1}$ is mass above the crack, $\vec{v}_{i,1}$ is velocity above the crack, $\vec{v}_{i,c}$ is the center-of-mass velocity of the two velocity fields, $\hat{n}_i$ and $\hat{t}_i$ are normal and tangent vectors to the crack surface, and Δt is the time step. By conservation of momentum, opposite forces are applied to the bottom of the crack. These forces correspond to forcing the two surfaces to move in the same center-of-mass velocity field and thus to stick together.

During frictional contact, the normal forces are the same, but the tangential forces differs. First the normal and tangential forces for stick conditions are calculated. If the stick values satisfy $|f_{i,T}| < \mu |f_{i,N}|$. where μ is the coefficient of friction, then the contact has not overcome friction and stick conditions are used. Otherwise, the tangential force is calculated from a friction law such that $f_{i,T} = \mu f_{i,N}$. All calculations in this paper used frictionless conditions for which $f_{i,T} = 0$ for all contact situations. In frictionless contact, contact only leads to normal forces.

Few of the results in this paper were influenced by crack contact effects. Nevertheless, contact calculations are needed to define the complete 3D CRAMP algorithm. Some results on pure mode II fracture in Nairn (2006) have shown that these contact methods correctly model cracks in contact.